

EXPERIMENTAL AND THEORETICAL INVESTIGATION OF TENSION STIFFENING AND CURVATURE IN RC BEAMS WITH EXTENDED CONCRETE COVER

Aleksandr SOKOLOV¹, Domas VALIUKAS², Mariyam PRALIYEVA³,
Amarjeet KUMAR², Darius BACINSKAS², Gintaris KAKLAUSKAS²

¹Laboratory of Innovative Building Structures, Vilnius Gediminas Technical University, Saulėtekio al. 11, LT-10223, Vilnius, Lithuania

²Department of Reinforced Concrete Structures and Geotechnical Engineering, Vilnius Gediminas Technical University, Saulėtekio al. 11, LT-10223, Vilnius, Lithuania

³Department of Construction and Building Materials, Satbayev University, Satbayev str. 22, 050013 Almaty, Kazakhstan

Article History:

- received 13 June 2024
- accepted 26 January 2025

Abstract. Accurate assessment of tension stiffening is important for predicting deflection and crack width in RC structures. Earlier studies by the authors have shown that an extended cover thickness increases tension stiffening in bending RC members. The current study experimentally and theoretically investigates curvature and tension stiffening in RC beams nominally having a 50 mm cover for 32 mm bars of tensile reinforcement. The four-point bending tests were carried out on square section (400×400 mm) RC beams. Mean experimental curvatures were obtained for the pure bending zone by different approaches, namely, from a mid-point deflection and from strains at several horizontal layers measured either by LVDT or DIC technique. The tension stiffening effect in the test beams was quantified by inversely calculating the resultant internal force of tensile concrete, N_{ct} , using the test moment – curvature diagrams. Tension stiffening is characterized by parameter β_0 indicating the ratio of $\beta_0 = M / M_{cr}$ at which the force N_{ct} reaches zero. The condition $N_{ct} = 0$ represents the bending stiffness of a fully cracked RC section. Earlier studies by the authors have shown that parameter β_0 equals to 3 for the beams with a typical cover thickness (25–35 mm). The current study has demonstrated that for the beams having nominal cover thickness of 50 mm and bar diameter of 32 mm, parameter β_0 reached rather high values indicating a little degradation of tension stiffening with increasing load.

Keywords: reinforced concrete, curvature, strain, deflection, test, tension stiffening, inverse analysis.

✉Corresponding author. E-mail: aleksandr.sokolov@vilniustech.lt

1. Introduction

The phenomenon of tension stiffening is critical in reinforced concrete (RC) structures (Lee, 2022; Pulatsu et al., 2021), as it significantly influences the serviceability and durability (Ng et al., 2020; Pulatsu et al., 2021) by affecting deflections and crack widths (Sakalauskas & Kaklauskas, 2023) under loading. Tension stiffening refers to the contribution of concrete in tension between cracks, which interacts with the embedded reinforcement to enhance the stiffness of RC members. This interaction is crucial in controlling crack development and propagation, thus maintaining the structural integrity and aesthetic appearance of concrete structures (Aryanto & Winata, 2021; Daud et al., 2021).

Numerous models were suggested to deal with tension stiffening. These models can be divided into four main groups:

- 1) Simplified semi-empirical models that incorporate tension stiffening via the effective geometrical characteristics. The code deflection models belong to this group (American Concrete Institute [ACI], 2019; European Committee for Standardization [CEN], 2023). The simplified models always use the plane section assumption. They generally use the geometrical characteristics of non-cracked and fully cracked RC section (Bischoff, 2005; Scanlon & Bischoff, 2008).

- 2) Tension stiffening models expressed via average stress – average strain law for cracked tensile concrete (Kaklauskas & Ghaboussi, 2001).
- 3) Tension stiffening models expressed via average stress – average strain law attributed to the tensile reinforcement. The approach was first proposed by Gilbert and Warner (1978) and further developed by Kaklauskas et al. (2011), Torres et al. (2015), Kaklauskas and Gribniak (2016).
- 4) Models based on the stress transfer approach (Lackner & Mang, 2003; Wu & Gilbert, 2009; Kaklauskas et al., 2012).

Quantifying the tension stiffening effect is a highly complex issue. While deriving tension stiffening laws based on the above approaches 2) and 3) is straightforward for tensile RC members, this is not the case for bending members. Kaklauskas and Ghaboussi (2001) proposed an inverse approach for deriving tension stiffening stress-strain relations for cracked tensile concrete based on the experimental moment – curvature response of RC bending members. This approach was further developed by Kaklauskas (2004), Torres et al. (2004), and Kaklauskas and Gribniak (2011). The latter study took into account the shrinkage effect on tension stiffening. Similar inverse constitutive modelling techniques were developed using the tension stiffening approach attributed to reinforcement (Kaklauskas et al., 2011; Torres et al., 2015; Kaklauskas & Gribniak, 2016). These approaches were further developed for deflection of RC members (Kaklauskas & Sokolov, 2021).

The above inverse techniques rely on accurate test data of RC members. New technologies, like Distributed Optical Fiber Sensors (DOFS) (Bado & Casas, 2021; Bado et al., 2021a, 2021b, 2022; Berrocal et al., 2021) and Digital Image Correlation (DIC) open up new prospects in acquiring highly accurate results in recording strain and displacement. Besides the traditional strain measuring techniques, the present research employs Digital Image Correlation (DIC), an advanced, cost-effective, and non-contact optical method for assessing displacement and strain. This technique operates by analyzing digital images of a component or specimen captured at various deformation stages. The device measures the displacement of the surface and creates strain maps and 2D and 3D deformation vector fields by tracking blocks of pixels in a complicated stochastic pattern. To determine the displacements and deformations, DIC compares the recorded values between the deformed and un-deformed pictures using a correlation method.

Previous research has demonstrated that various parameters, such as the thickness of the concrete cover and the diameter of the reinforcement bars, significantly impact the tension stiffening effect (Gribniak et al., 2016; Martin et al., 2020; Ng et al., 2020; Kumar et al., 2019). For instance, studies have indicated that an increased cover thickness can enhance tension stiffening, thereby improving the performance of RC members in bending (Fantilli

et al., 2021; Hung et al., 2019). Recent advancements in the field of fiber-reinforced concrete (FRC) have opened new avenues for enhancing the tension stiffening effect (Daud et al., 2021). FRC incorporates fibrous materials such as steel, glass, synthetic, or natural fibers, which are distributed throughout the concrete matrix. These fibers bridge cracks and provide additional tensile strength and stiffness, reducing the dependency on conventional steel reinforcement. The synergy between fibers and traditional reinforcement can lead to significant improvements in the performance of concrete structures (Teng et al., 2022), especially under flexural and tensile loads (Kaklauskas et al., 2024; Lee, 2022).

This study aims to expand the current understanding of tension stiffening by experimentally and theoretically examining RC beams with specific reinforcement configurations. By focusing on beams with a 50 mm cover for 32 mm bars of tensile reinforcement, the research seeks to quantify the tension stiffening effect through detailed four-point bending tests. The results will be analyzed using inverse calculation methods to determine the internal tensile concrete forces, providing insights into the curvature and tension stiffening behavior of the tested beams. In addition to the experimental approach, this study will incorporate advanced techniques such as Digital Image Correlation (DIC) and Linear Variable Differential Transformers (LVDTs) to measure strains and curvatures accurately. These methods will help validate the experimental findings and ensure the reliability of the tension stiffening models developed.

2. Test program

2.1. Description of beam specimens

Two nominally identical concrete beams, named as B1 and B2, were reinforced with 32 mm bars. The beams of square section (400×400 mm) were tested under a four-point bending scheme. The beams were 1.7 m long (1.6 m in span) with a 0.6 m pure bending zone and two shear zones, each 0.5 m long. Both the tensile zone and the compression zone were reinforced with two 32 mm bars each. The shear zone was reinforced with 10 mm steel stirrups spaced at 30 mm. The pure bending zone had no shear reinforcement to exclude the effect of stirrups on cracking. Main geometrical and material characteristics of the beams are presented in Figure 1 and Table 1. Due to some differences in section height, h , and effective depth, d , cover, c , for the tensile reinforcement also slightly differed, being 52 mm and 50 mm for beams B1 and B2, respectively.

Table 1. Main characteristics of RC specimens

Specimen	h , mm	b , mm	d , mm	d_{scr} , mm	c , mm	A_{sr} , mm ²	A_{scr} , mm ²	ρ , %
B1	402	401	334	78	52	1608	1608	1.19
B2	405	424	339	81	50	1608	1608	1.12

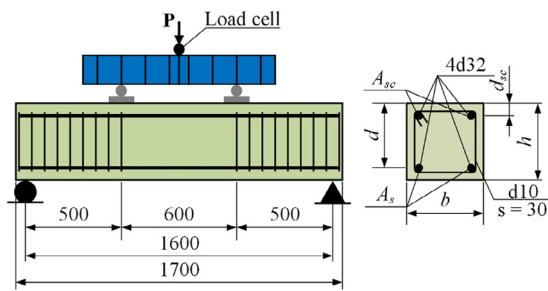


Figure 1. Four-point bending tests of RC beams

2.2. Materials

Both beams were produced the same day from the same concrete mix. The components of concrete mix are given in Table 2. Water-cement ratio was 0.5. The experimental beams were cast using timber formworks and were un-moulded 3 days after casting. The specimens were cured at an average relative humidity (RH) of 73% and a temperature of 20 °C. The beams were tested at 150 days after casting. Concrete compressive strength was defined from standard cylinder ($\varnothing 150 \times 300$) mm tests at 28 days after the casting and at the time of testing. The tensile strength of concrete was determined from the flexural test of concrete prisms of $100 \times 100 \times 400$ mm dimensions. Main mechanical test characteristics of concrete are given in Table 3 along with the modulus of elasticity, E_c , assessed by CEB-FIP (2020). The uniaxial tests were performed on the steel bars of diameters 32 mm and 10 mm. Table 4 gives modulus of elasticity, E_s , and yield strength, f_y , of the flexural tensile reinforcement (32 mm bars). Testing of a 32 mm bar is illustrated in Figure 2.

2.3. Test setup and instrumentation

The loading setup and instrumentation is depicted in Figure 3. The load was applied via a displacement-controlled 5000 kN servohydraulic testing machine with a loading rate of 0.4 mm/min. A steel beam was used to distribute the load from the servohydraulic cylinder to the beam.

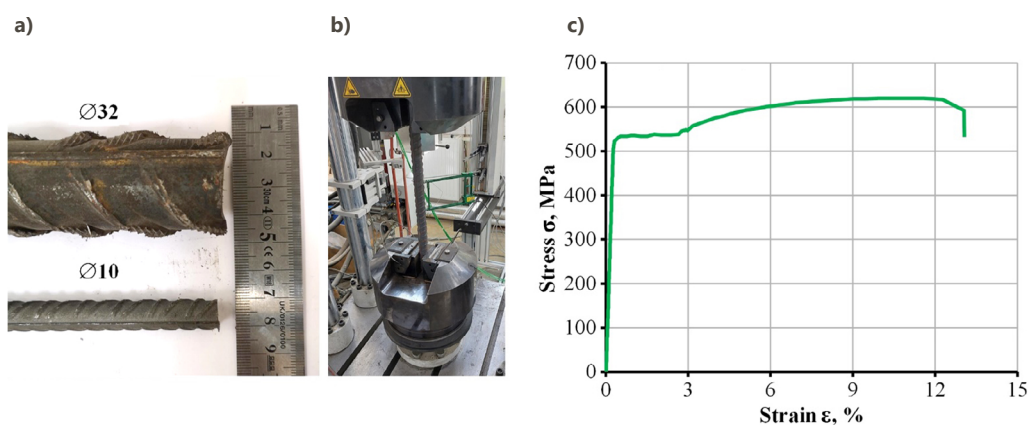


Figure 2. Testing of a steel bar: a – a surface shape; b – general view; c – stress–strain diagram of a 32 mm bar

Table 2. Components of concrete mix [kg/m^3]

Chemical composition	Quantity
Ordinary Portland Cement (CEM I 42.5 N)	400
Water-cement ratio 0.5	200
Fine aggregate 0/4 mm	750
Crushed coarse aggregate 4/16 mm	1166

Table 3. Mechanical properties of steel bars

Diameter of steel bar (mm)	Yield stress (MPa)	Ultimate stress (MPa)	Modulus of elasticity of reinforcement (MPa)
10	500	625	202855
32	520	656	198046

Table 4. Mechanical properties of concrete

Age (days)	Cylinder strength (MPa)	Modulus of elasticity of concrete (MPa)	Flexural strength (MPa)
28	41.9	33820	6.01
150	49.2	35477	8.36

Deflections of the beams were measured at three points (the mid-span and the points of load application) by linear variable differential transformers (LVDT) placed under the beams (see Figure 3). Three LVDT's were used at each of the points. LVDT's were also used to measure average concrete surface strains within the length of the pure bending zone (0.6 m). The LVDT's were placed on one side of the beam at four equally spaced horizontal lines (two along the centroid of the bottom and top reinforcement and two in between). Every strain recording line consisted of three LVDT's, each covering a 200 mm distance. The other side of the beams (different from the one where the surface strains were measured) was used to record cracks. The crack pattern was marked during the tests. Crack width was measured in two ways – using an electronic microscope and the digital image correlation (DIC) technique.



Figure 3. A general view of the test setup: a – DIC equipment; b – beam view; c – surface strain measurement using LVDT

3. Test ultimate load, strains and curvatures

Beam B1 was tested until the ultimate bending moment $M_u = 282$ kNm was reached. Beam B2 was tested until $M = 276$ kNm, just before reaching the ultimate load. The test was terminated to safeguard the measuring devices from damage that may happen at failure of the beam.

Average concrete surface strains with increasing bending moment are shown in Figures 4a and 4b for beams B1 and B2, respectively. These figures depict the mean strains ε_{ij} recorded by every LVDT placed at four horizontal lines (see Figure 3c). The subscript i ($i = 1 \dots 4$) of strain ε_{ij} refers to the number of the horizontal line, whereas the subscript j ($j = 1 \dots 3$) indicates the number of a specific LVDT within the horizontal line i . It is evident that index $i = 1$ represents the extreme compressive strains and index $i = 4$ refers to the mean concrete strains of the centroid of the tensile reinforcement.

While in general the moment–strain diagrams shown in Figures 4a and 4b are clustered in the groups representing a specific horizontal line i , there is some scatter in the strains within the same line i , but having different number j . This is in particular noticeable for the maximum tensile strains that might be significantly affected by individual cracks. The effect of cracks on the compressive strains is less clear. The surface strain recordings obtained by each of the LVDT were used to define the average curvature. First, strains were averaged along each horizontal line. Sec-

ond, the averaged strains were used to calculate curvature by the formula:

$$\kappa = \frac{1}{6} \sum_{\substack{k < m \\ k=1;2;3}} \frac{\varepsilon_k - \varepsilon_m}{y_{k,m}}, \quad (1)$$

where ε_k and ε_m are the averaged strains along lines k and m , respectively; $y_{k,m}$ is the distance between lines k and m .

Curvature via Eqn (1) is expressed as the difference of strains at two horizontal lines divided by the distance between the respective lines, $y_{k,m}$. Eqn (1) calculates the average of six possible combinations of pairing different strain lines. To be specific, line 1 is paired with lines 2, 3 and 4, line 2 is paired with lines 3 and 4, and line 3 is paired with line 4.

The moment–curvature diagrams obtained by Eqn (1) are shown in red colour in Figures 5a and 5b for beams B1 and B2, respectively. Figure 6 depicts these two figures compared to each other and excellent agreement can be noted. Figures 5a and 5b also show other moment–curvature diagrams obtained by alternative approaches. Curvature graphs shown in yellow colour were obtained from a deflection within the pure bending zone under the assumption of constant curvature within this zone. Two more moment–curvature graphs were obtained using the DIC technique and are described below:

- 1) The first DIC setup included two LAVISION VC-IMAGE E-LITE 5M cameras with a 2456×2085 pixel

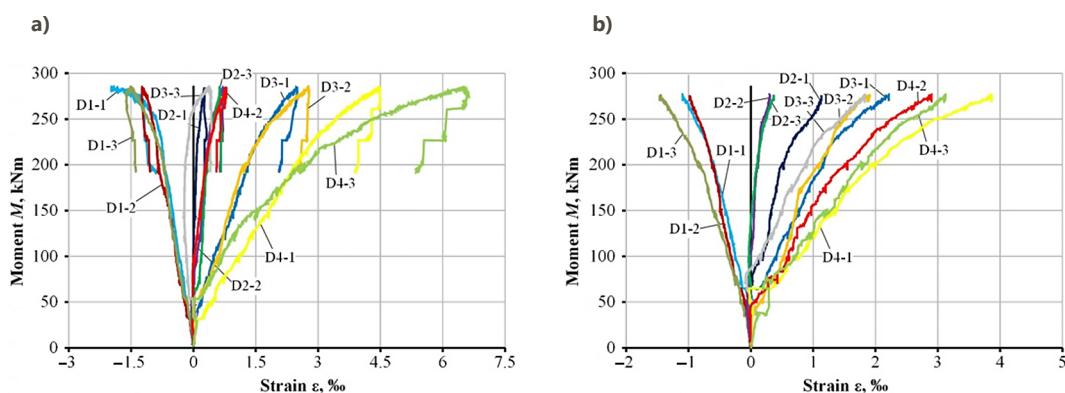


Figure 4. Moment–strain diagrams recorded by LVDT placed along four horizontal lines within the pure bending zone: a – beam B1; b – beam B2

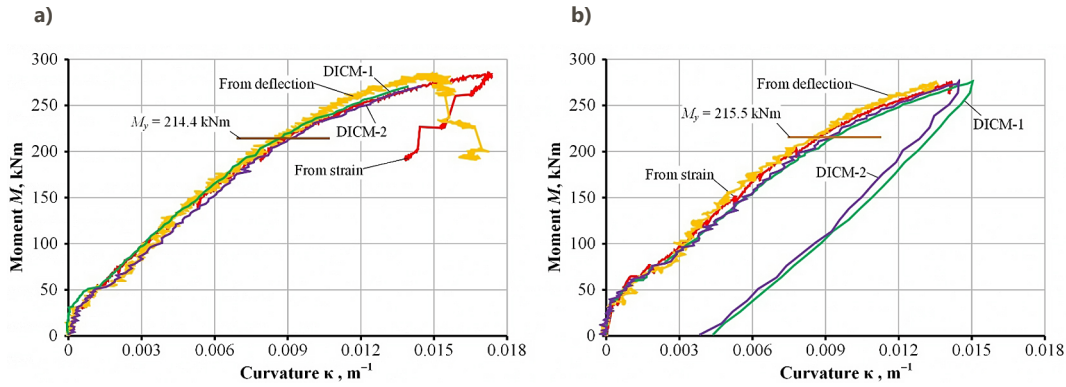


Figure 5. Moment–curvature diagrams for beams B1 and B2

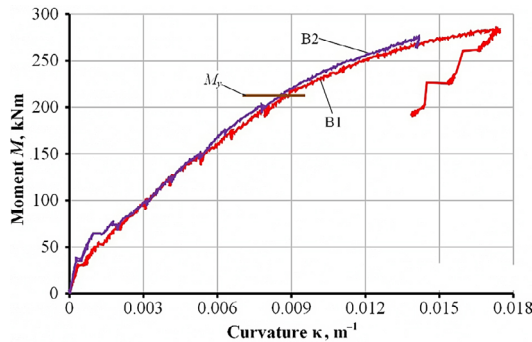


Figure 6. Comparison of moment–curvature diagrams for beams B1 and B2

resolution placed 0.5 m apart from each other and 3m away from the test beam. The camera operates at 12.2 frames per second. To ensure quality of the digital images, lighting ARRI equipment was used. The longitudinal surface strains were obtained at two levels (tensile and compressive reinforcement) based on the displacement recordings along the pure bending zone at three intervals 200 mm each. The moment–curvature diagrams (see Figures 5a and 5b) by this approach are shown in green colour.

- 2) The second DIC setup employed a CANON digital single-lens reflex camera with a resolution of 6000×4000 pixels. The settings of the camera were as follows: exposure time = 1/200 s, aperture = f/4.5, sensitivity to light = ISO 100, and focal length = 24 mm. Similarly to the above approach, strains were obtained at two levels, namely, along the tensile and compressive reinforcement. The difference from the above was that the strain was obtained from the displacement between the end points of the pure bending zone being 600 mm apart, instead of three distances 200 mm each. The moment–curvature graphs by this approach are given in violet colour (Figures 5a and 5b).

The moment–curvature diagrams calculated by the four approaches in general well agree with each other. It is rather difficult to judge which of the approaches is most accurate. It could be guessed that the graph obtained from the pure bending zone deflections is the least accu-

rate. This graph is the least smooth (has most scattering) and has extended load intervals being most distant from the other relations. The graphs obtained by DIC have a good agreement with each other, particularly for beam B2, when even the unloading parts are close. In terms of accuracy, the winner could be the moment–curvature graph obtained from the recordings of LVDT placed at four levels. Another possibility of the most accurate experimental graph could be the averaged moment–curvature obtained by several approaches but excluding the one obtained from deflections.

4. Quantifying tension stiffening

Tension stiffening is investigated using an inverse technique proposed by the authors and other investigators (Kaklauskas et al., 2011; Torres et al., 2015; Kaklauskas & Gribniak, 2016; Kaklauskas & Sokolov, 2021). The method considers a RC member subjected to bending as shown in Figure 7. Plane section hypothesis implying linear strain distribution (Figure 7b) is adopted. Elastic properties are assumed for compressive concrete. Figure 7c shows the internal forces of compressive concrete (N_c), compressive reinforcement (N_{sc}), tensile reinforcement (N_s) and tensile concrete (N_{ct}). The latter represents concrete stresses due to tension stiffening and tension softening effects. As suggested by Gilbert and Warner (1978), the force N_{ct} is applied at the centroid of the tensile reinforcement (Figure 7c).

The main idea of the method is calculating the resultant force of tensile concrete from an experimental moment–curvature diagram. The governing equation of the inverse technique has the following form (Kaklauskas et al., 2024):

$$\kappa \frac{E_c y_c^2 b}{2} \left(d - \frac{y_c}{3} \right) + \kappa E_{sc} (d - d_{sc}) (y_c - d_{sc}) A_{sc} - M = 0, \quad (2)$$

where E_c is the concrete Young's modulus, E_{sc} is the modulus of elasticity of the top steel bars, d is the effective depth to the tensile steel area, d_{sc} is the effective depth to the compressive reinforcement, b is the width of the cross section and A_{sc} is the area of the compressive reinforcement.

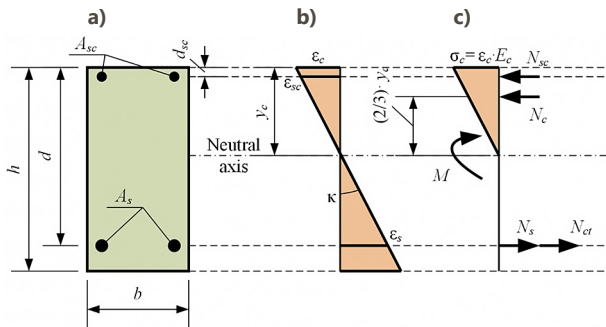


Figure 7. Strains, stresses and internal forces in the inverse technique: a – an RC beam section; b – strain distribution; c – stresses and internal forces

In Eqn (2), bending moment, M , and curvature, κ , are taken from the experiment. Eqn (2) is a third order equation with the compressive depth, y_c , being the only unknown. After the above equation is solved and compressive depth, y_c is defined, the internal force of tensile concrete can be calculated by Eqn (3) (Kaklauskas et al., 2024). The resultant internal force can be then expressed from:

$$N_{ct} = \kappa \left[\frac{E_c y_c^2 b}{2} + E_{sc} (y_c - d_{sc}) A_{sc} - E_s (d - y_c) A_s \right]. \quad (3)$$

The above technique and the experimental curvatures calculated from the strains recorded at four horizontal lines using LVDT (Figure 6) were employed to calculate the resultant internal force of tensile concrete N_{ct} . Figure 8 depicts the force N_{ct} variation for beams B1 and B2 in respect to the normalized bending moment expressed as M / M_{cr} . M_{cr} was calculated according to ACI (American Concrete Institute, 2014, 2019) (see Eqn (7)). According to Kaklauskas and Sokolov (2021), the graphs of N_{ct} versus M / M_{cr} can be idealized by a bilinear shape: within the elastic stage, it linearly increases from zero to a maximum value reached at approximately $M / M_{cr} = 1$ and then almost linearly goes down crossing the horizontal axis at $M / M_{cr} = \beta_0$. The factor β_0 has an important physical meaning. It represents the bending moment $\beta_0 M_{cr}$ at which the RC member has the bending stiffness equivalent to the that of the fully cracked section. The study by Kaklauskas and Sokolov (2021) has shown that for RC beams having a typical cover thickness (25 to 35 mm), the parameter β_0 approximately equals to

3. The mentioned reference has also noted that parameter β_0 might be significantly larger for RC members having an extended cover. This is clearly the case for the current test beams. As can be seen from Figure 8a, the degradation in tension stiffening with increasing bending moment is very insignificant. The figure shows an averaged linear approximation of the N_{tc} graphs for beams B1 and B2 within the M / M_{cr} range between 1 and 4.8, with the latter representing the yielding bending moment. After the trendline is extended further than $M / M_{cr} = 4.8$, it crosses the horizontal coordinate at $\beta_0 = 27.6$ (see Figure 8b). This is significantly more than $\beta_0 = 3$ taken for typical covers. In fact, the test beams under investigation demonstrate the tension stiffening behavior similar to that of steel fibre reinforced beams (Gribniak et al., 2016; Kaklauskas et al., 2022; Meskenas et al., 2021) when little degradation of stresses in tensile concrete takes place.

The reasons of slow degradation of tension stiffening are not fully clear and need further investigation. One of the main reasons could be a relatively large clear cover (nominally 50 mm). The beams having the section height of 400 mm are expected to have secondary cracks between the primary cracks (Kaklauskas et al., 2024). However, as shown in Figure 9, the test beams due to a large cover basically do not have secondary cracks that significantly add to the damage of tension stiffening. Another reason could be a large bar diameter (32 mm), which along with the cover is responsible for an extended crack spacing and thus less damage of tension stiffening.

If N_{ct} is taken equal to 0 and is removed from Figure 7c, the figure will represent the internal forces of the fully cracked RC section. It could be reminded that stiffness of a fully cracked section, $E_c I_{cr}$ can be easily calculated by standard formulas.

5. Predicting curvatures and deflections

In this section, curvatures are predicted using a model proposed by Kaklauskas and Sokolov (2021). As shown in Figure 10, the model has two characteristic points: point 1 represents the cracking bending moment, $M_1 = M_{cr}$ and respective curvature $\kappa_1 = M_{cr} / (E_c I)$; and point 2 represents the bending moment $M_2 = \beta_0 M_{cr}$ and the curvature κ_2 cal-

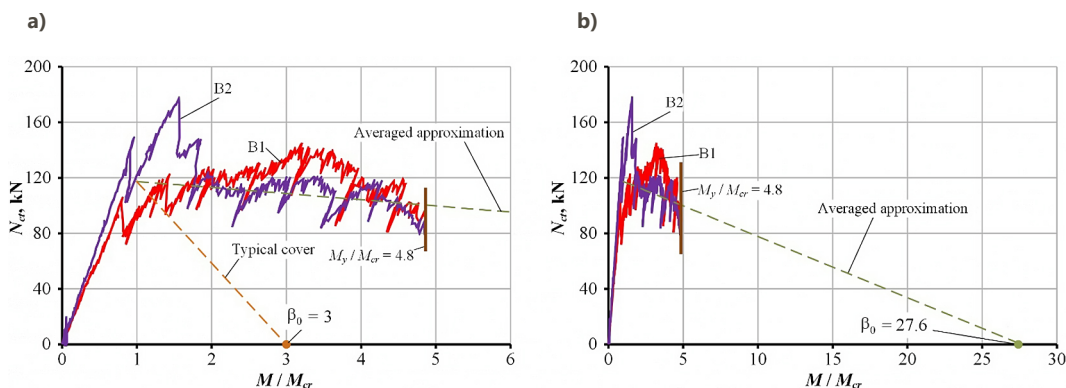


Figure 8. The inversely calculated internal force of tensile concrete, N_{ct} : a – N_{ct} forces for beams B1 and B2; b – identifying parameter β_0

culated as $\kappa_2 = \beta_0 M_{cr} / (E_c I_{cr})$ where I_{cr} represents the moment of inertia of the fully cracked section. Then curvature of cracked RC member is calculated by linearly connecting points 1 and 2 (Kaklauskas & Sokolov, 2021):

$$\kappa = \kappa_1 + (\kappa_2 - \kappa_1) (M / M_1 - 1) / (\beta_0 - 1); \quad (4)$$

$$\kappa_1 = M_{cr} / E_c I; \quad (5)$$

$$\kappa_2 = \beta_0 M_{cr} / E_c I_{cr}. \quad (6)$$

The cracking bending moment, M_{cr} , is defined by the formula of ACI 318-14 (American Concrete Institute, 2014) and ACI 318-19 (American Concrete Institute, 2019):

$$M_{cr} = f_r I_g / y_t, \quad (7)$$

where y_t is the distance from the centroid of the section to the tension face ($y_t = 0.5h$ for a rectangular section); f_r is

the concrete rupture modulus, for normal-weight concrete calculated as (American Concrete Institute, 2019):

$$f_r = 0.623 (f_c)^{0.5}, \quad (8)$$

where f_c is the cylinder strength in MPa.

The above curvature model uses the elasticity modulus of concrete suggested by ACI 318-19 (American Concrete Institute, 2019):

$$E_c = 4700 (f_c)^{0.5}. \quad (9)$$

The moment–curvature diagrams predicted by Eqn (4) for beams B1 and B2 are shown in Figure 11 along with the test graphs. Parameter $\beta_0 = 27.6$ as obtained from the inverse analysis is used. Good agreement between the predicted and test results can be stated.

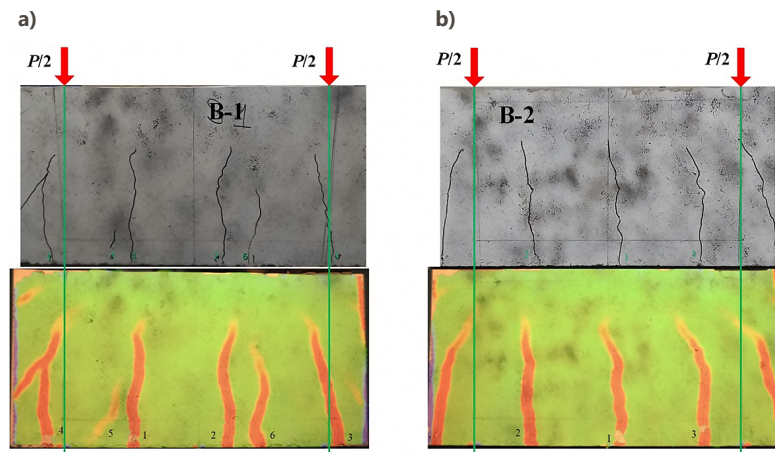


Figure 9. The final crack patterns: a – beam B1; b – beam B2

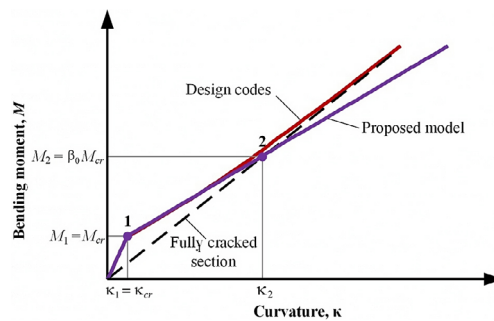


Figure 10. The curvature model

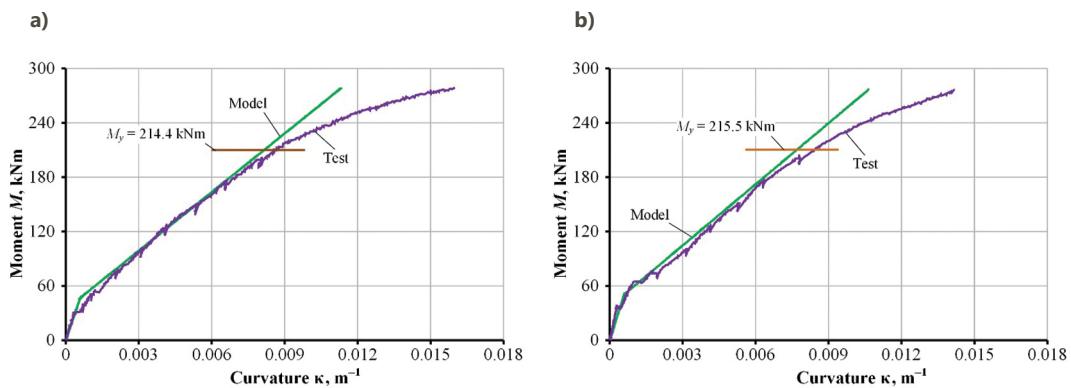


Figure 11. Predicted versus test moment–curvature diagrams: a – beam B1; b – beam B2

6. Conclusions

- The constitutive modelling of tension stiffening was carried out by inverse approach using test moment–curvature relationships. Tension stiffening was quantified in a simple way using a resultant internal force of tensile concrete applied at the centroid of tensile reinforcement.
- Having accurate experimental moment – curvature diagrams is fundamental in obtaining reliable tension stiffening modelling results. For that most suitable experiment is a four-point test of RC beam with extended pure bending zone.
- Mean experimental curvatures within the pure bending zone were obtained by three different approaches: 1) from a deflection of the pure bending zone; 2) from strains at several horizontal layers along the pure bending zone recorded by LVDT; 3) from strains at several horizontal layers measured using the DIC technique. While the agreement of the moment–curvature relationships obtained by the different techniques was good, the approach of measuring strains at several horizontal layers using LVDT could be preferred. The other two approaches may also be used for accurate moment–curvature extraction.
- The robustness of the inverse approach is demonstrated by a good agreement of the calculated internal tensile concrete force for the twin test specimens.
- The resultant tensile force N_{tc} linearly increases from zero bending moment and reaches a maximum value at M_{cr} and then descends.
- Tension stiffening in bending members can be quantified by parameter β_0 indicating the ratio of $\beta_0 = M / M_{cr}$ at which the resultant tensile force N_{ct} reaches zero. The condition $N_{ct} = 0$ represents the bending stiffness of a fully cracked RC section which disregards stresses in the tensile concrete. The larger is parameter β_0 , the more significant is tension stiffening.
- Earlier studies by the authors of RC bending members have shown that parameter β_0 equals to 3 if: 1) M_{cr} is calculated by ACI code, and 2) the beams have a typical cover thickness (25–35 mm) of the tensile reinforcement. The current study has demonstrated that for the test beams having bar diameter 32 mm and nominal cover thickness 50 mm, the resultant tensile force N_{ct} had little degradation with increasing normalized bending moment, M / M_{cr} , that resulted in an increased value of parameter β_0 .

Acknowledgements

The authors gratefully acknowledged the financial support provided by the Research Council of Lithuania for project No. P-MIP-23-386. This work was supported by Project No. 101121210 “City Nature-Based Solutions Integration to Local Urban Infrastructure Protection for a Climate Resilient Society” (NBSINFRA) from the European Union’s Horizon Europe program.

Disclosure statement

The authors declare no conflict of interests.

References

- American Concrete Institute. (2014). *Building code requirements for structural concrete and commentary* (ACI 318-14). https://www.concrete.org/store/productdetail.aspx?ItemID=318U14&Language=English&Units=US_Units
- American Concrete Institute. (2019). *Building code requirements for structural concrete and commentary* (ACI 318-19). https://www.concrete.org/store/productdetail.aspx?ItemID=318U19&Language=English&Units=US_Units
- Aryanto, A., & Winata, B. J. (2021). Tension stiffening behavior of polypropylene fiber-reinforced concrete tension members. *Journal of Engineering and Technological Sciences*, 53(2), Article 210209. <https://doi.org/10.5614/j.eng.technol.sci.2021.53.2.9>
- Bado, M. F., & Casas, J. R. (2021). A review of recent distributed optical fiber sensors applications for civil engineering structural health monitoring. *Sensors*, 21(5), Article 1818. <https://doi.org/10.3390/s21051818>
- Bado, M. F., Casas, J. R., Dey, A., Berrocal, C. G., Kaklauskas, G., Fernandez, I., & Rempling, R. (2021a). Characterization of concrete shrinkage induced strains in internally-restrained RC structures by distributed optical fiber sensing. *Cement and Concrete Composites*, 120, Article 104058. <https://doi.org/10.1016/j.cemconcomp.2021.104058>
- Bado, M. F., Casas, J. R., & Kaklauskas, G. (2021b). Distributed sensing (DOFS) in reinforced concrete members for reinforcement strain monitoring, crack detection and bond-slip calculation. *Engineering Structures*, 226, 24–29. <https://doi.org/10.1016/j.engstruct.2020.111385>
- Bado, M. F., Tonelli, D., Poli, F., Zonta, D., & Casas, J. R. (2022). Digital twin for civil engineering systems: An exploratory review for distributed sensing updating. *Sensors*, 22(9), Article 3168. <https://doi.org/10.3390/s22093168>
- Berrocal, C. G., Fernandez, I., Bado, M. F., Casas, J. R., & Rempling, R. (2021). Assessment and visualization of performance indicators of reinforced concrete beams by distributed optical fibre sensing. *Structural Health Monitoring*, 20(6), 2899–3452. <https://doi.org/10.1177/1475921720984431>
- Bischoff, P. H. (2005). Reevaluation of deflection prediction for concrete beams reinforced with steel and fiber reinforced polymer bars. *ASCE Journal of Structural Engineering*, 131(5), 752–767. [https://doi.org/10.1061/\(ASCE\)0733-9445\(2005\)131:5\(752\)](https://doi.org/10.1061/(ASCE)0733-9445(2005)131:5(752))
- CEB-FIP. (2020). *CEB-FIP model code 2020: Model code for concrete structures*. <https://www.fib-international.org/publications/model-codes.html>
- Daud, R. A., Daud, S. A., & Azzawi, A. A. (2021). Tension stiffening evaluation of steel fiber concrete beams with smooth and deformed reinforcement. *Journal of King Saud University – Engineering Sciences*, 33, 147–152. <https://doi.org/10.1016/j.jksues.2020.03.002>
- European Committee for Standardization. (2023). *Eurocode 2: Design of concrete structures – Part 1-1: General rules and rules for buildings* (EN 1992-1-1:2023). <https://www.en-standard.eu/bs-en-1992-1-1-2023-eurocode-2-design-of-concrete-structures-general-rules-and-rules-for-buildings-bridges-and-civil-engineering-structures/>
- Fantilli, A. P., Orfeo, B., & Caldentey, A. P. (2021). The deflection of reinforced concrete beams containing recycled steel fibers. *Structural Concrete*, 22, 2089–2104. <https://doi.org/10.1002/suco.202000729>

- Gilbert, R. I., & Warner, R. F. (1978). Tension stiffening in reinforced concrete slabs. *ASCE Journal of the Structural Division*, 104(12), 1885–1900.
[https://doi.org/10.1061/\(ASCE\)0733-9445\(2007\)133:6\(899\)](https://doi.org/10.1061/(ASCE)0733-9445(2007)133:6(899))
- Gribniak, V., Perez, C. A., Kaklauskas, G., Rimkus, A., & Sokolov, A. (2016). Effect of arrangement of tensile reinforcement on flexural stiffness and cracking. *Engineering Structures*, 124, 418–428. <https://doi.org/10.1016/j.engstruct.2016.06.026>
- Hung, C. C., Lee, H. S., & Chan, S. N. (2019). Tension-stiffening effect in steel-reinforced UHPC composites: Constitutive model and effects of steel fibers, loading patterns, and rebar sizes. *Composites Part B*, 158, 269–278.
<https://doi.org/10.1016/j.compositesb.2018.09.091>
- Kaklauskas, G. (2004). Flexural layered deformational model of reinforced concrete members. *Magazine of Concrete Research*, 56(10), 575–584. <https://doi.org/10.1680/macr.2004.56.10.575>
- Kaklauskas, G., & Ghaboussi, J. (2001). Stress-strain relations for cracked tensile concrete from RC beam tests. *ASCE Journal of Structural Engineering*, 127(1), 64–73.
[https://doi.org/10.1061/\(ASCE\)0733-9445\(2001\)127:1\(64\)](https://doi.org/10.1061/(ASCE)0733-9445(2001)127:1(64))
- Kaklauskas, G., & Gribniak, V. (2011). Eliminating shrinkage effect from moment-curvature and tension-stiffening relationships of reinforced concrete members. *ASCE Journal of Structural Engineering*, 137(12), 1460–1469.
[https://doi.org/\(ASCE\)ST.1943-541X.0000395](https://doi.org/(ASCE)ST.1943-541X.0000395)
- Kaklauskas, G., & Gribniak, V. (2016). Hybrid tension stiffening approach for decoupling shrinkage effect in cracked reinforced concrete members. *ASCE Journal of Engineering Mechanics*, 142(11), Article 04016085.
[https://doi.org/10.1061/\(ASCE\)EM.1943-7889.0001148](https://doi.org/10.1061/(ASCE)EM.1943-7889.0001148)
- Kaklauskas, G., & Sokolov, A. (2021). A peculiar value of M to M_{cr} ratio: Reconsidering assumptions of curvature analysis of reinforced concrete beams. *Applications in Engineering Science*, 7, Article 100053. <https://doi.org/10.1016/j.apples.2021.100053>
- Kaklauskas, G., Gribniak, V., Salys, D., Sokolov, A., & Meskenas, A. (2011). Tension stiffening model attributed to tensile reinforcement for concrete flexural members. *Procedia Engineering*, 14, 1433–1438. <https://doi.org/10.1016/j.proeng.2011.07.180>
- Kaklauskas, G., Gribniak, V., Jakubovskis, R., Gudonis, E., Salys, D., & Kupliauskas, R. (2012). Serviceability analysis of flexural reinforced concrete members. *Journal of Civil Engineering and Management*, 18(1), 24–29.
<https://doi.org/10.3846/13923730.2011.643553>
- Kaklauskas, G., Sokolov, A., Shakeri, A., Ng, P. L., & Barros J. A. O. (2022). Curvature-based analysis of concrete beams reinforced with steel bars and fibres. *Structural Engineering and Mechanics*, 81(3), 349–365. <https://doi.org/10.12989/sem.2022.81.3.349>
- Kaklauskas, G., Sokolov, A., & Barros, J. A. O. (2024). A design methodology for fiber reinforced concrete elements in serviceability conditions integrating tension softening and stiffening effects. *Engineering Structures*, 311, Article 118199.
<https://doi.org/10.1016/j.engstruct.2024.118199>
- Kumar, V. S., Indira, P. V., & Ganesan, N. (2019). Tension stiffening and cracking behaviour of hybrid fibre reinforced ternary blend geopolymers concrete. *Journal of Structural Engineering*, 46(4), 257–266.
- Lackner, R., & Mang, H. A. (2003). Scale transition in steel-concrete interaction. Part I: Model. *ASCE Journal of Engineering Mechanics*, 129(4), 393–402.
[https://doi.org/10.1061/\(ASCE\)0733-9399\(2003\)129:4\(393\)](https://doi.org/10.1061/(ASCE)0733-9399(2003)129:4(393))
- Lee, J. D. (2022). The effect of tension stiffening in moment-curvature responses of prestressed concrete members. *Engineering Structures*, 257, Article 114043.
<https://doi.org/10.1016/j.engstruct.2022.114043>
- Martin, M. P., Rangel, C. S., Amario, M., Lima, J. M. F., Lima, P. R. L., & Filho, R. D. T. (2020). Modelling of tension stiffening effect in reinforced recycled concrete. *Revista IBRACON de Estruturas e Materiais*, 13(6), Article e13605.
<https://doi.org/10.1590/S1983-41952020000600005>
- Meskenas, A., Ramanauskas, R., Sokolov, A., Bacinskas, D., & Kaklauskas, G. (2021). Residual stress-strain relations inversely derived from experimental moment-curvature response of RC beams with fibres compared to the recommendations of design codes. *Structures*, 34, 3363–3375.
<https://doi.org/10.1016/j.istruc.2021.09.070>
- Ng, P. L., Barros, J. A. O., Kaklauskas, G., & Lam J. Y. K. (2020). Deformation analysis of fiber-reinforced polymer reinforced concrete beams by tension-stiffening approach. *Composite Structures*, 234, Article 111664.
<https://doi.org/10.1016/j.compstruct.2019.111664>
- Pulatsu, B., Erdogan, E., Lourenco, P. B., Lemos, J.V., & Tuncay, K. (2021). Numerical modeling of the tension stiffening in reinforced concrete members via discontinuum models. *Computational Particle Mechanics*, 8, 423–436.
<https://doi.org/10.1007/s40571-020-00342-5>
- Sakalauskas, K., & Kaklauskas, G. (2023). Pure shear model for crack width analysis of reinforced concrete members. *Scientific Reports*, 13(1), Article 13883.
<https://doi.org/10.1038/s41598-023-41080-x>
- Scanlon, A., & Bischoff, P. H. (2008). Shrinkage restraint and loading history effects on deflection of flexural members. *ACI Structural Journal*, 105(4), 498–506. <https://doi.org/10.14359/19864>
- Teng, L., Zhang, R., & Khayat, K. H. (2022). Tension-stiffening effect consideration for modeling deflection of cracked reinforced UHPC beams. *Sustainability*, 14(1), Article 415.
<https://doi.org/10.3390/su14010415>
- Torres, L., Lopez-Almansa, F., & Bozzo, L. M. (2004). Tension-stiffening model for cracked flexural concrete members. *ASCE Journal of Structural Engineering*, 130(8), 1242–1251.
[https://doi.org/10.1061/\(ASCE\)0733-9445\(2004\)130:8\(1242\)](https://doi.org/10.1061/(ASCE)0733-9445(2004)130:8(1242))
- Torres, L., Barris, C., Kaklauskas, G., & Gribniak, V. (2015). Modeling of tension-stiffening in bending RC elements based on equivalent stiffness of the rebar. *Structural Engineering and Mechanics*, 53(5), 997–1016.
<https://doi.org/10.12989/sem.2015.53.5.997>
- Wu, H. Q., & Gilbert, R. I. (2009). Modeling short-term tension stiffening in reinforced concrete prism using a continuum-based finite element model. *Engineering Structures*, 31(10), 2380–2391. <https://doi.org/10.1016/j.engstruct.2009.05.012>